

**Supplementary materials to:
Charting human subcortical maturation across the adult
lifespan with *in vivo* 7 T MRI**

Steven Miletić^{a,1,*}, Pierre-Louis Bazin^{a,b,1}, Scott J. S. Isherwood^a, Max C. Keuken^a,
Anneke Alkemade^{a,2}, Birte U. Forstmann^{a,2,*}

^{1,2}Authors contributed equally

^aUniversity of Amsterdam, Department of Psychology, Integrative Model-based Cognitive Neuroscience research unit (IMCN), Nieuwe Achtergracht 129B, Amsterdam, The Netherlands

^bMax Planck Institute for Human Cognitive and Brain Sciences, Departments of Neurophysics and Neurology, Stephanstraße 1A, Leipzig, Germany

*Corresponding authors:

Steven Miletić, Nieuwe Achtergracht 129B, 1001 NK Amsterdam, The Netherlands, s.miletic@uva.nl

Birte U. Forstmann, Nieuwe Achtergracht 129B, 1001 NK Amsterdam, The Netherlands, buforstmann@gmail.com

Declarations of interest: None

CNR comparisons

Under the assumption of mono-exponential signal decay, the expected contrast-to-noise ratio (CNR) of an $T2^*$ -weighted single echo, echo planar imaging protocol, per unit change in $T2^*$, is given by (e.g. Poser et al., 2006; Posse et al., 1999):

$$CNR(TE, T2^*) = \frac{S_0}{\sigma_0} TE \exp \frac{-TE}{T2^*} \quad (1)$$

where S_0 and σ_0 are the signal and (temporal) variance, respectively, at echo time $TE = 0$. In the following comparisons, we assume that S_0 and σ_0 are the same across structures and protocols. This assumption is unlikely to be true for between-region CNR comparisons, as S_0/σ_0 is typically lower in subcortical regions compared to cortical regions in part due to the larger distance to the MRI receiver coils. We ignore any potential between-region differences in the size of the $T2^*$ changes that result from changes in the oxygenation levels. Under these assumptions, CNR ratios can be used to compare the expected CNRs when using echo time A to study region n with the expected CNR when using echo time B to study region m :

$$\frac{CNR(TE_A, T2_m^*)}{CNR(TE_B, T2_n^*)} = \frac{TE_A \exp \frac{-TE_A}{T2_m^*}}{TE_B \exp \frac{-TE_B}{T2_n^*}} \quad (2)$$

First, we can compare the expected CNR in the red nucleus with the CNR in the amygdala, both in 19 years old participants, using $T2^*$ values obtained through our app (<https://subcortex.eu/app>). Filling in $TE_A = TE_B = T2_{amyg}^* = 0.04248$ s (i.e., in both protocols, we use an echo time optimized for the amygdala at 19 years old), and $T2_{rn}^* = 0.01825$ s, we find $\frac{CNR(TE_A, T2_{rn}^*)}{CNR(TE_B, T2_{amyg}^*)} = 0.265$, implying the CNR in the red nucleus is approximately 73.5% lower than in the amygdala with this echo time. In practice, since S_0/σ_0 is also likely to be lower in the red nucleus than in the amygdala, the CNR ratio will be even lower.

Second, we can estimate the effect of age-related decreases in $T2^*$. The red nucleus has an approximate $T2^* = 0.01825$ s at 19 years old, and $T2^* = 0.0131$ s at 50 years old. If an echo time of $TE_A = TE_B = 0.01825$ s is used for a participant of 50 years old, then $\frac{CNR(0.01825, 0.0131)}{CNR(0.01825, 0.01825)} = 0.6765$, showing an approximately 32% loss in CNR compared to the CNR that would be obtained with this echo time in a participant of 19 years old.

Third, we can compare the expected CNR in the red nucleus at 19 years old ($T2^* = 0.01825$ s) when using the optimal echo time $TE_A = 0.01825$ s with the CNR that would be obtained if an echo time is used that is optimal for the amygdala: $TE_B = 0.04248$ s.

The ratio $\frac{CNR(0.01825,0.01825)}{CNR(0.04248,0.01825)} = 1.621$, showing that a substantial CNR gain can be expected from optimising the echo time to meet the specific requirements of that region.

Finally, we can compare the effect of adapting echo times to adjust for age-related changes in $T2^*$. Taking again the red nucleus as an example, the $T2^*$ decreases from 0.01825 s to 0.0131 s between 19 and 50 years old. Suppose we analyze the red nucleus in a 50 year old participant using the corresponding optimal echo time (hence, $TE_A = T2^* = 0.0131$ s), then, compared with using an echo time optimal for young participants $TE_B = 0.01825$ s, we find that $\frac{CNR(0.0131,0.0131)}{CNR(0.01825,0.0131)} = 1.063$. Hence, adjusting for the age-related decrease in $T2^*$ leads to modest CNR gains.

In practice, changing the echo time may not always be possible due to hardware limitations (e.g., the slew rate of the MRI gradients limits the minimum echo time that can be achieved), and potentially requires undersampling of k-space (e.g., using GRAPPA, SENSE, or partial Fourier) or bandwidth changes. These additional changes will affect the protocols' S_0/σ_0 , complicating direct comparison between the expected performance of two candidate MRI protocols. Another option is to use multi echo protocols, in which data is acquired at multiple echo times, which can be optimized for multiple regions at the same time (Gowland & Bowtell, 2007; Kundu et al., 2017; Miletic et al., 2020; Puckett et al., 2018). These additional factors should be taken into account when developing an MRI protocol in order to find the optimal trade-off between echo time settings and S_0/σ_0 .

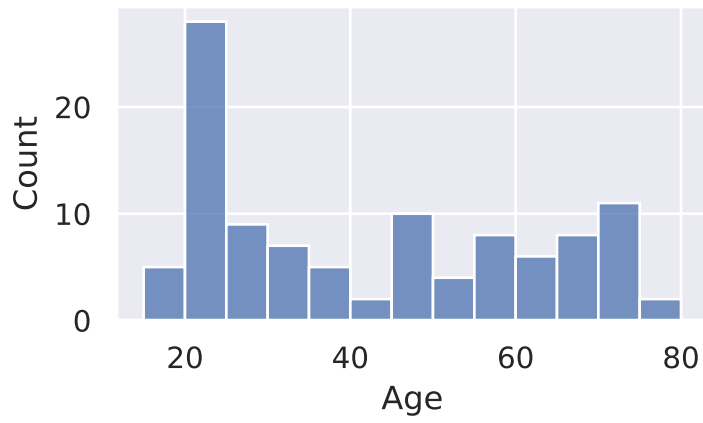


Figure S1: Distribution of ages of all participants. The breaks of the bins are at every 5 years between 20–75 years old.

Table S1: Iron estimates and corresponding qMRI values used for estimating the linear models that relate iron concentrations to qMRI values. For all regions that were divided in subregions in one but not the other source (i.e. GP vs GPi/GPe; STR vs PUT/CAU; brain stem vs medulla oblongata; and cortical areas), we entered all subregions in the OLS model, using the more specific values where possible, and the global values otherwise. E.g., both GPe and GPi were in the model and shared iron values (Hallgren and Sourander report only GP), but different qMRI values. To obtain qMRI values for cortex, brain stem, and cerebellum, we parcellated our qMRI data using MGDM and CRUISE Bazin et al. (2014) ^aFrom Hallgren and Sourander (1958); ^bFrom Metere and Möller (2018); ^cWe used the qMRI metrics of the internal capsule here

	Iron (ppm)	QSM (ppm)	R1 (Hz)	R2* (Hz)
Brainstem	1.4 ^a	-0.000486	0.808	37.959
CAU	9.28 ^a	0.012768	0.66	48.64
Cerebellum	3.35 ^a	$-7.80 * 10^{-5}$	0.505	34.069
Frontal Cortex	2.92 ^a	$-4.00 * 10^{-6}$	0.537	32.722
Frontal White	4.24 ^a	-0.020322 ^c	0.895 ^c	36.294 ^c
GPe	21.3 ^a	0.042671	0.848	85.107
GPi	21.3 ^a	0.047246	0.869	77.739
Motor Cortex	5.03 ^a	$-4.00 * 10^{-6}$	0.537	32.722
Occipital Cortex	4.55 ^a	$-4.00 * 10^{-6}$	0.537	32.722
PUT	13.32 ^a	0.012768	0.655	48.644
Parietal Cortex	3.81 ^a	$-4.00 * 10^{-6}$	0.537	32.722
RN	19.48 ^a	0.063051	0.922	74.041
SN	18.46 ^a	0.058915	0.862	72.284
Sensory Cortex	4.32 ^a	$-4.00 * 10^{-6}$	0.537	32.722
THA	4.76 ^a	0.002828	0.758	38.228
Temporal Cortex	3.13 ^a	$-4.00 * 10^{-6}$	0.537	32.722
VENT	0.062 ^b	0.005553	0.341	6.259

Table S2: Myelin estimates and corresponding qMRI values used for estimating the linear models that relate myelin concentrations to qMRI values. For all regions that were divided in subregions in one but not the other source (i.e. GP vs GPi/GPe; STR vs PUT/CAU; brain stem vs medulla oblongata; and cortical areas), we entered all subregions in the OLS model, using the more specific values where possible, and the global values otherwise. E.g., both CAU and PUT were in the model with separate myelin values, but identical qMRI values since the MASSP parcellation only reports STR. To obtain qMRI values for cortex, brain stem, and cerebellum, we parcellated our qMRI data using MGDM and CRUISE Bazin et al. (2014). ^aFrom Randall (1938); ^bFrom Metere and Möller (2018); ^cEstimated based on the *post mortem* specimen; ^dWe used the qMRI metrics of the internal capsule here.

	Myelin (ppm)	QSM (ppm)	R1 (Hz)	R2* (Hz)
Brainstem	15.36 ^a	-0.000486	0.808	37.959
CAU	6.21 ^a	0.012768	0.655	48.644
Frontal Cortex	5.08 ^a	-4.00 * 10 ⁻⁶	0.537	32.722
Frontal White	16.26 ^a	-0.020322 ^d	0.895 ^d	36.294 ^d
GPe	10.404 ^c	0.044293	0.813	84.875
GPi	10.404 ^c	0.046384	0.838	75.216
Parietal Cortex	5.42 ^a	-4.00 * 10 ⁻⁶	0.537	32.722
PUT	5.611 ^c	0.012768	0.655	48.644
RN	13.442 ^c	0.059001	0.894	72.979
SN	7.404 ^c	0.05624	0.846	71.532
STN	14.423 ^c	0.058185	0.935	78.924
THA	11.4 ^a	0.002828	0.758	38.228
VENT	0.002 ^b	0.005553	0.232	6.259

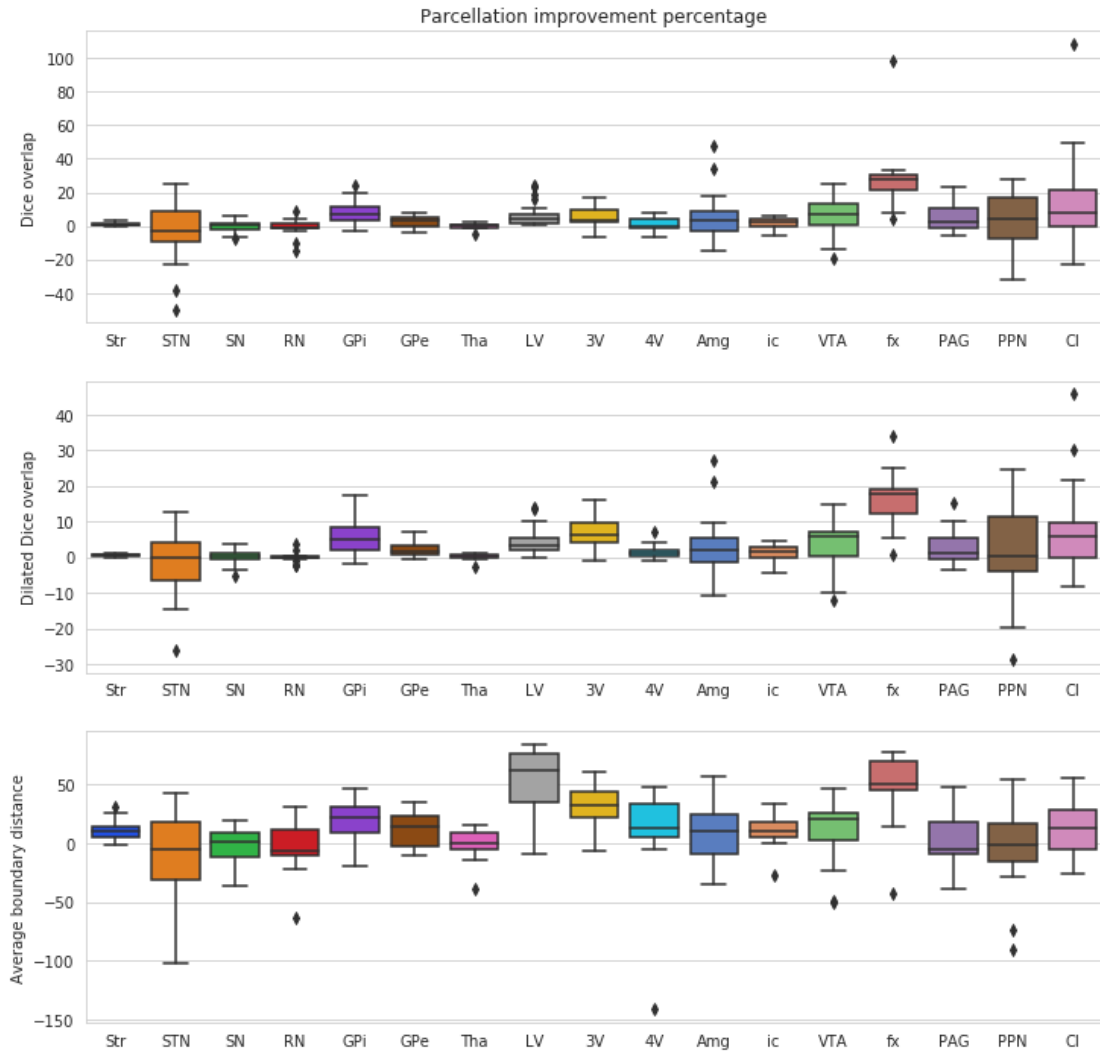


Figure S2: Leave-one-out re-validation of the MASSP algorithm. The boxplots show the percentage of improvement in parcellation accuracy of the version of MASSP in the current study (with a second co-registration and an intensity normalization step) compared to the original MASSP. Positive values indicate better values for the current version. The dilated Dice overlap coefficient is the Dice coefficient after dilating the masks by 1 voxel; as such, it provides a measure of overlap while allowing for 1 voxel of uncertainty. For full details on these metrics, see Bazin et al. (2020).

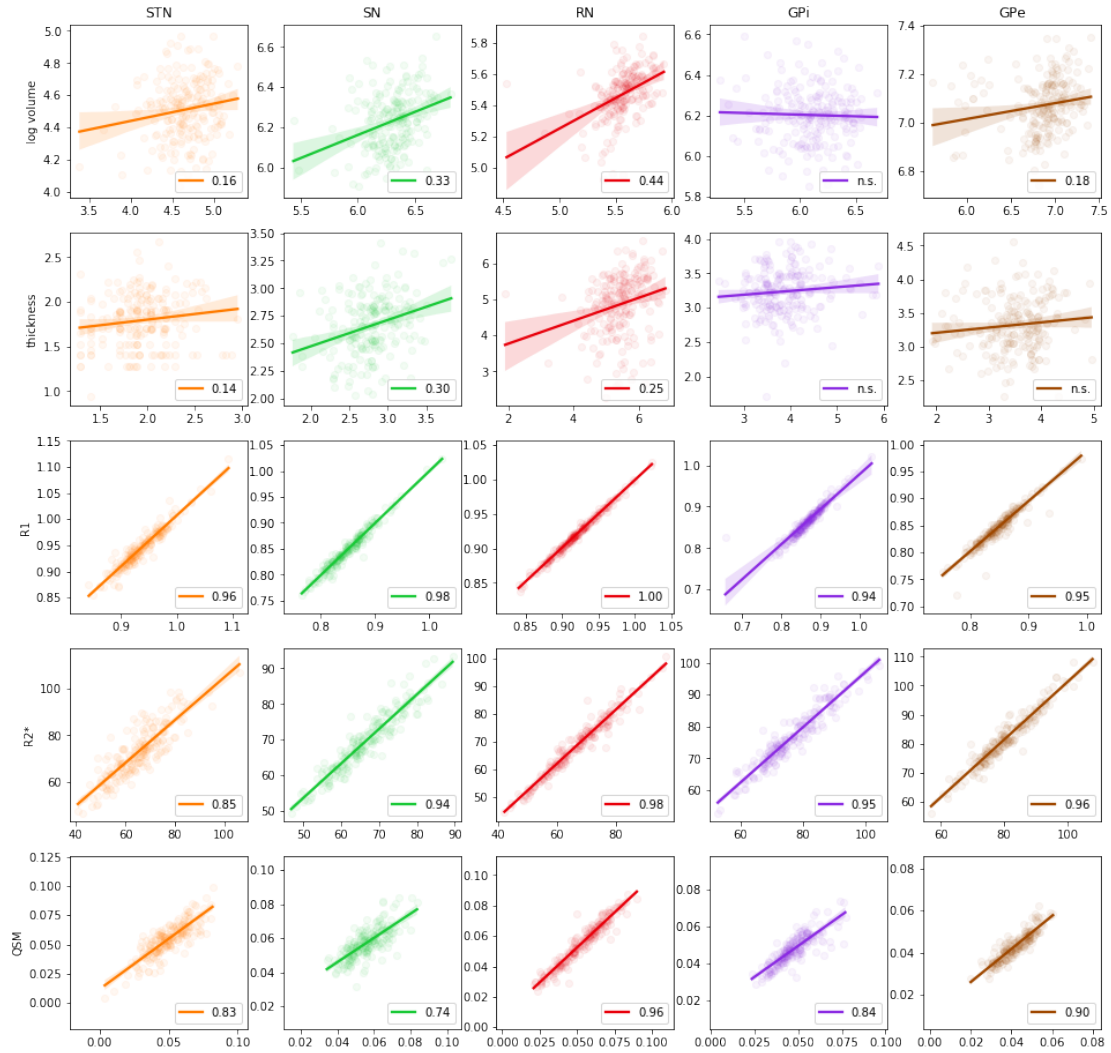


Figure S3: Comparison between metrics obtained by manual delineation (x-axes) with metrics obtained when using the improved version of MASSP to delineate structures. Rows indicate volume, thickness, R1, R2*, and QSM. Circles are individual data points, straight lines are regression lines with 95% confidence intervals as the shaded area. Pearson's correlation coefficients are shown when the correlation was significant.

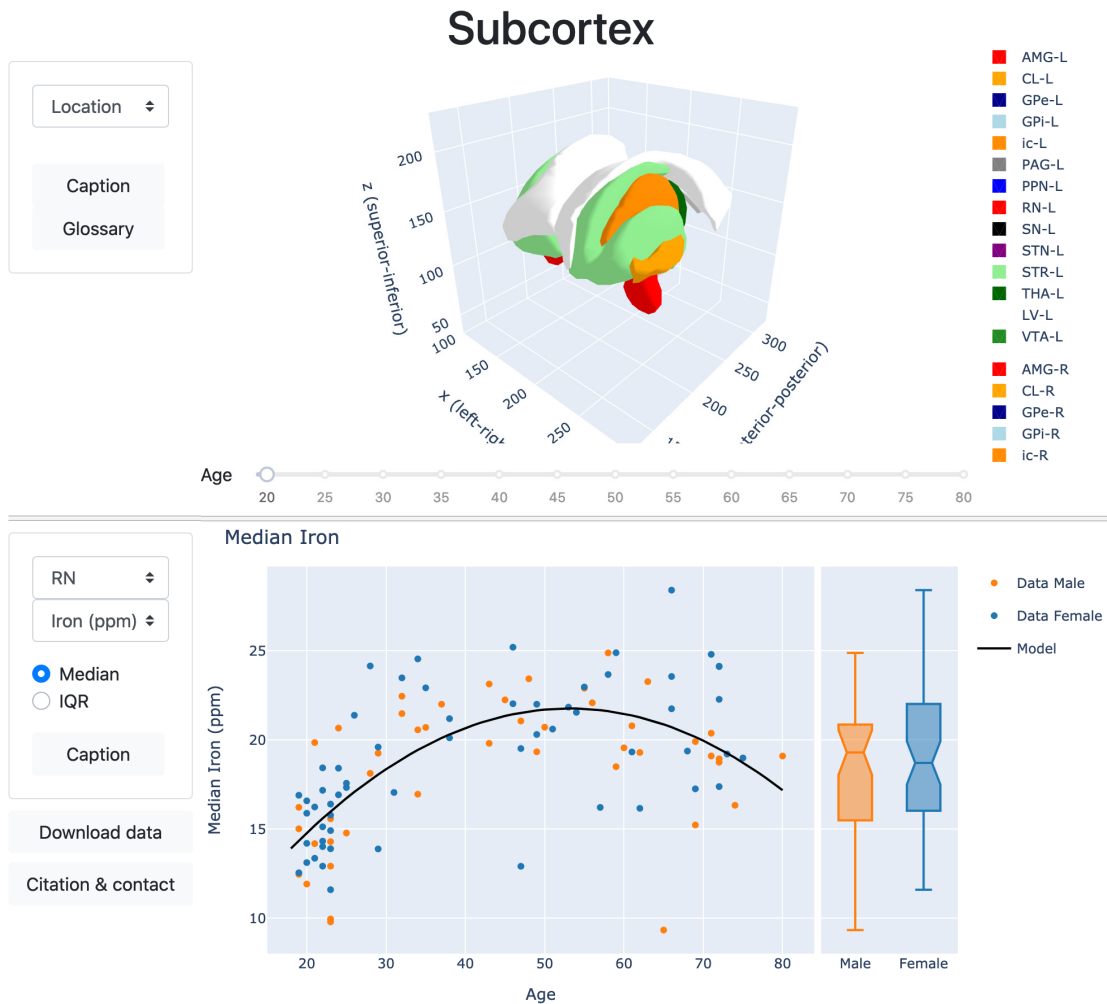


Figure S4: Illustration of the interactive app which allows for visualizing all data and age-related change models. Top panel features a 3D mesh plot that includes all 17 subcortical structures under investigation. The age slider can be used to visualize the age-related changes in center of mass location (currently visible), or the median or interquartile range of iron, myelin, R1, R2*, and QSM values, color-coded on the structures. Bottom panel features scatterplots of the relation between age and twelve measures (median and interquartile range of myelin, iron, R1, R2*, QSM, and thickness) for all structures. Optional captions are included, and the data underlying the bottom panel can readily be downloaded as a csv file. The app can be accessed via <https://subcortex.eu/app>

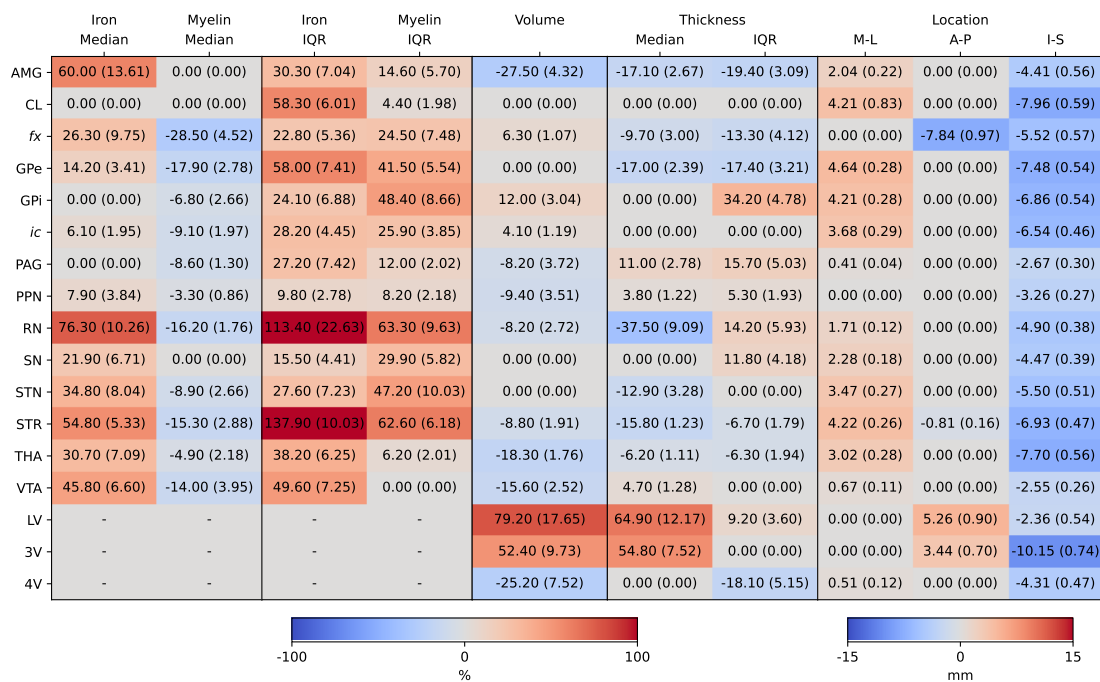


Figure S5: Matrix of total age-related change in all dependent variables (columns) for individual structures (rows). Values indicate the summed absolute change between 19-75 years old. Negative values indicate decreases. Standard errors were obtained by bootstrapping with 10,000 iterations and are shown in parentheses. The ventricular system is assumed to have no iron or myelin concentration and is excluded from analysis.

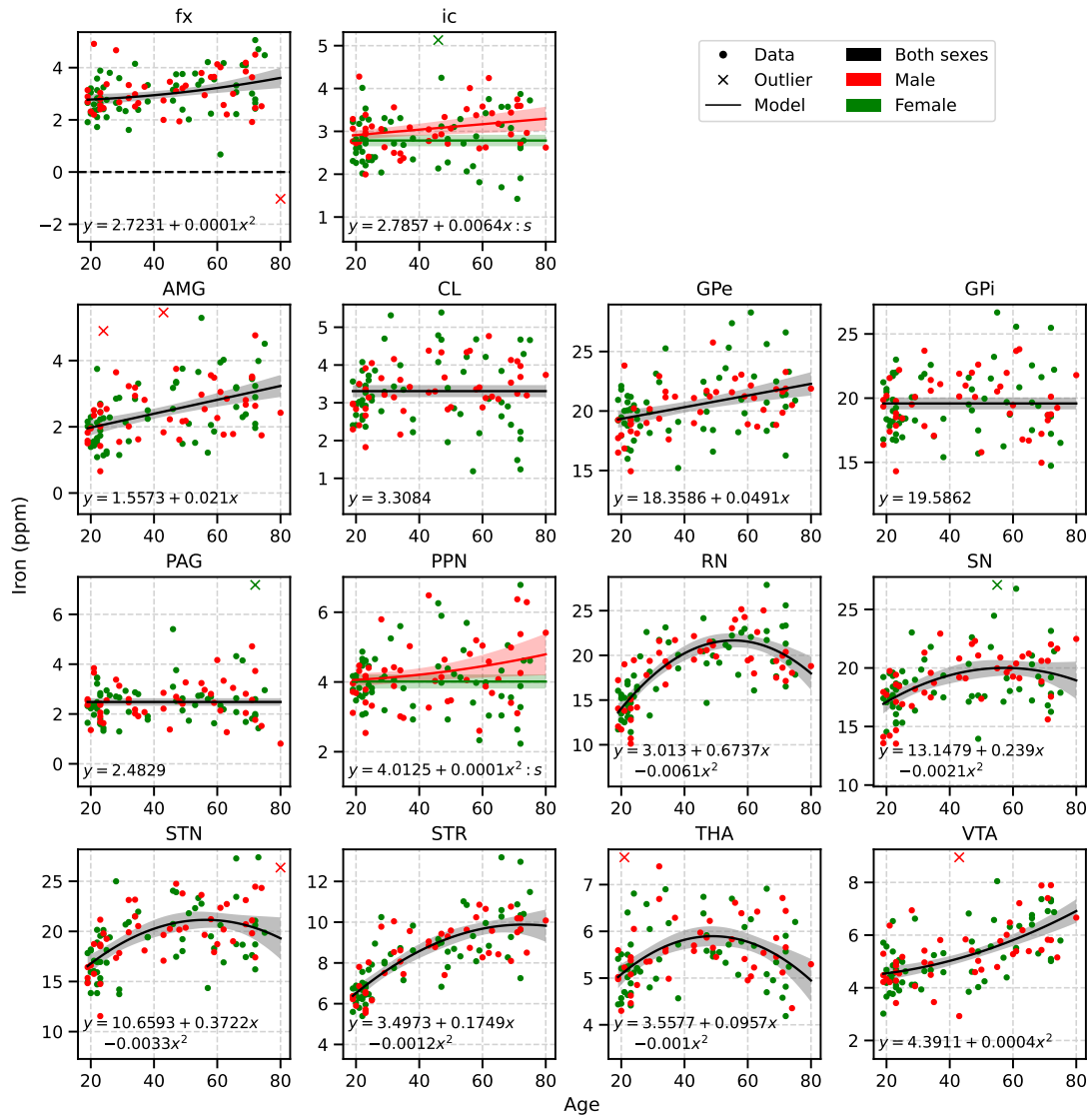


Figure S6: Age-related change in median iron for all structures. Equations are the parameterized winning models, with x referring to age, and s to sex (dummy coded; 0 = female, 1 = male), and colons indicate interactions. Shaded areas indicate 95% confidence intervals of the winning model predictions

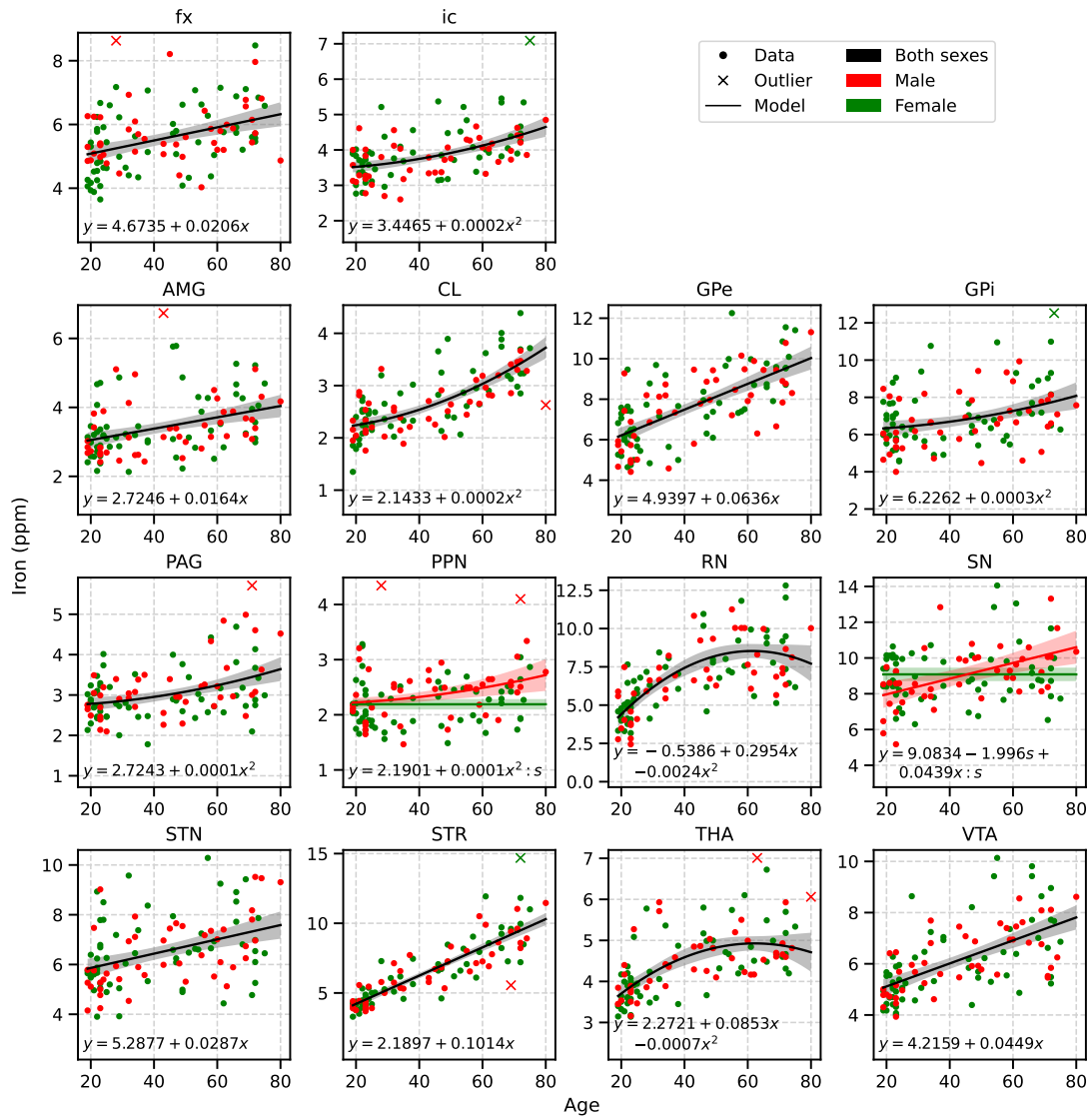


Figure S7: Age-related change in IQR iron for all structures. Equations are the parameterized winning models, with x referring to age, and s to sex (dummy coded; 0 = female, 1 = male), and colons indicate interactions. Shaded areas indicate 95% confidence intervals of the winning model predictions

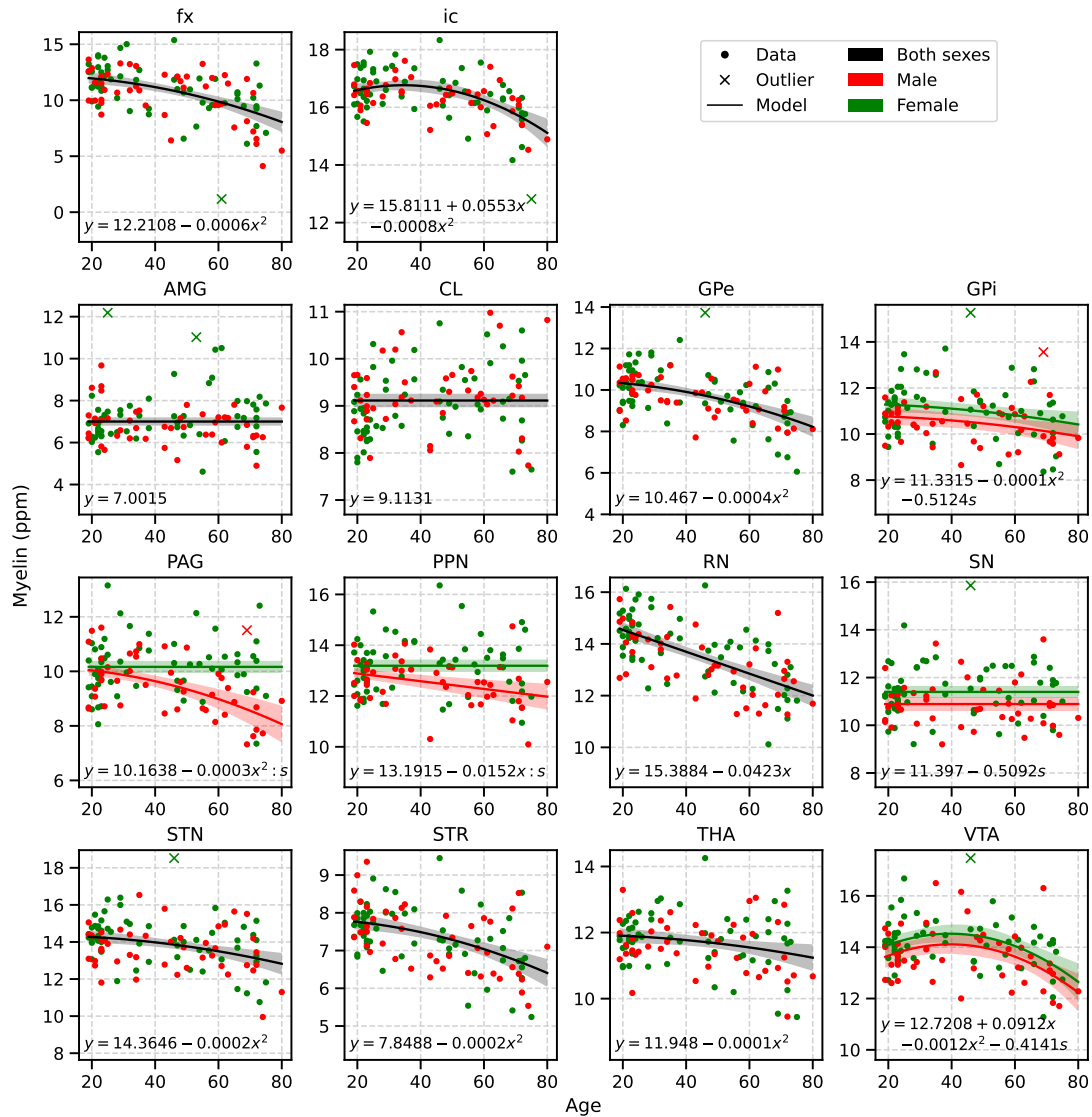


Figure S8: Age-related change in median myelin for all structures. Equations are the parameterized winning models, with x referring to age, and s to sex (dummy coded; 0 = female, 1 = male), and colons indicate interactions. Shaded areas indicate 95% confidence intervals of the winning model predictions

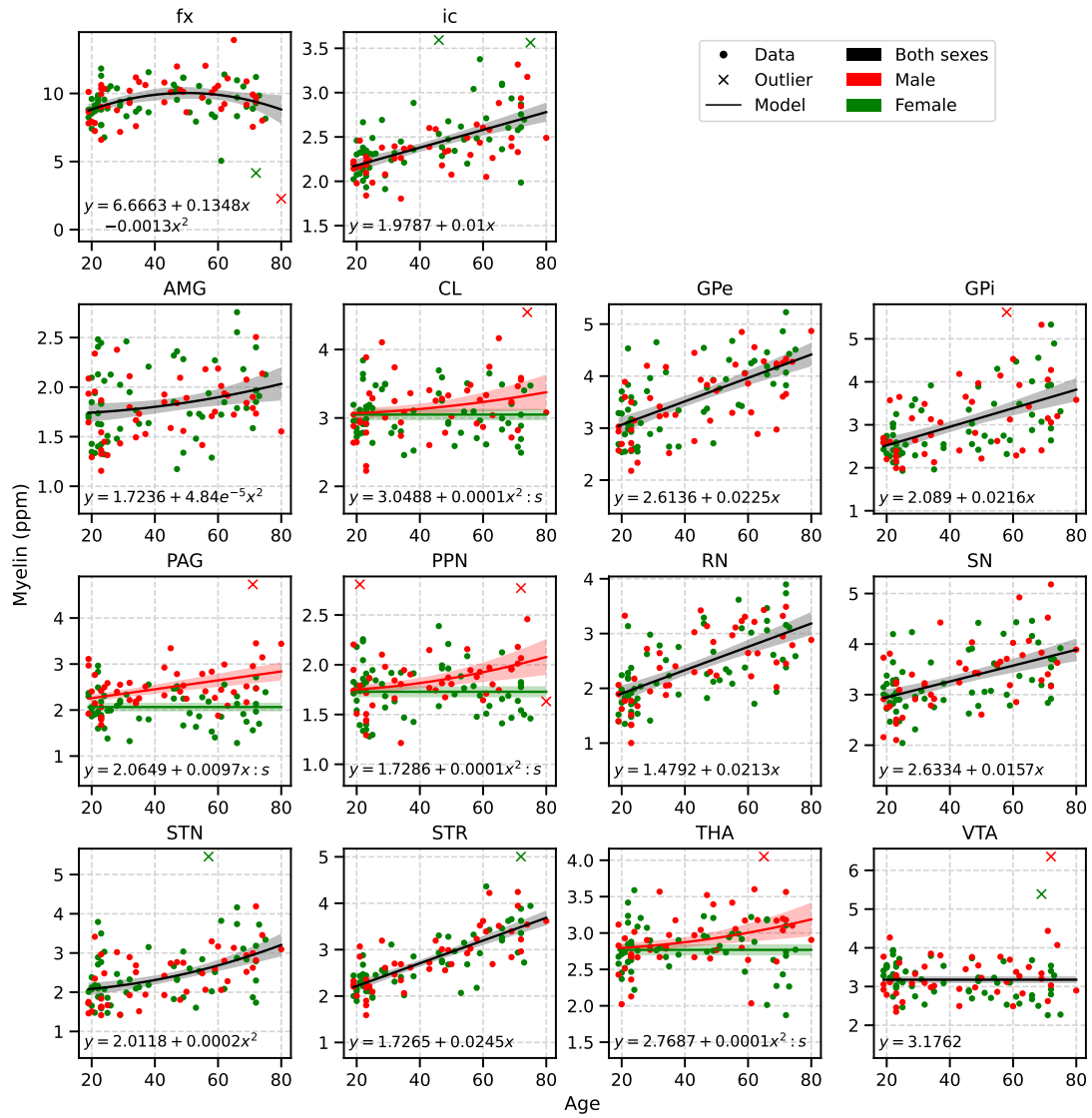


Figure S9: Age-related change in IQR myelin for all structures. Equations are the parameterized winning models, with x referring to age, and s to sex (dummy coded; 0 = female, 1 = male), and colons indicate interactions. Shaded areas indicate 95% confidence intervals of the winning model predictions

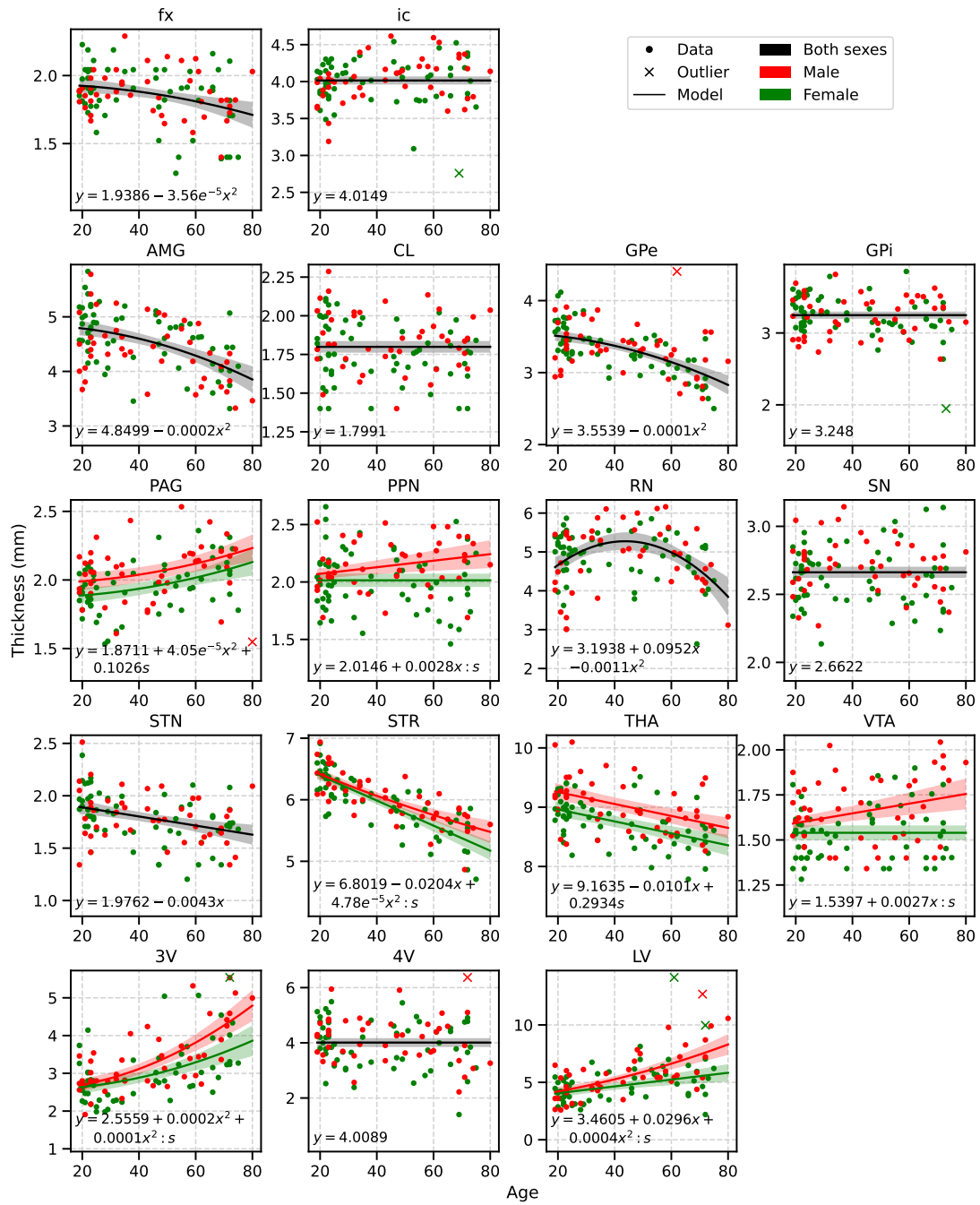


Figure S10: Age-related change in median thickness for all structures. Equations are the parameterized winning models, with x referring to age, and s to sex (dummy coded; 0 = female, 1 = male), and colons indicate interactions. Shaded areas indicate 95% confidence intervals of the winning model predictions

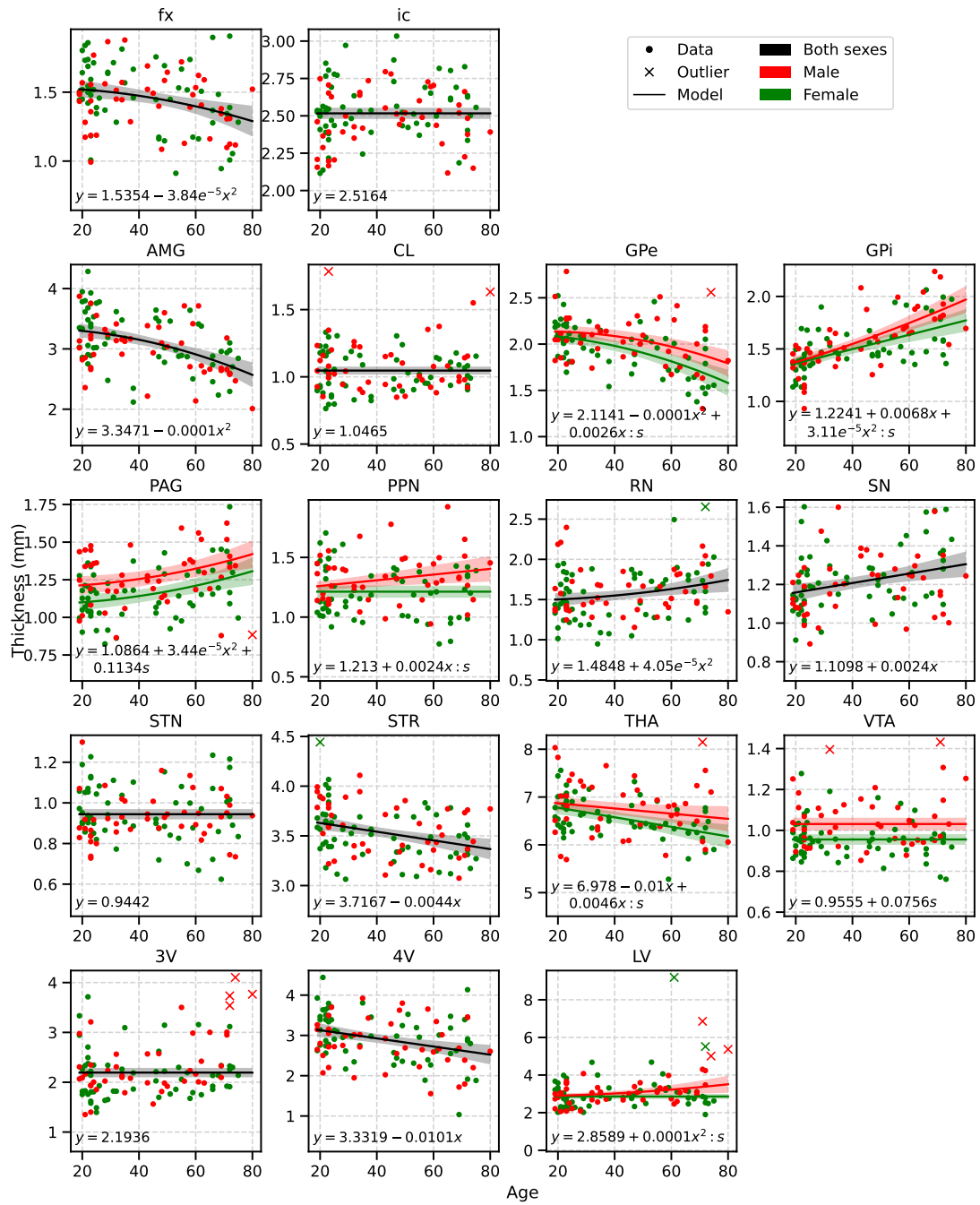


Figure S11: Age-related change in IQR thickness for all structures. Equations are the parameterized winning models, with x referring to age, and s to sex (dummy coded; 0 = female, 1 = male), and colons indicate interactions. Shaded areas indicate 95% confidence intervals of the winning model predictions

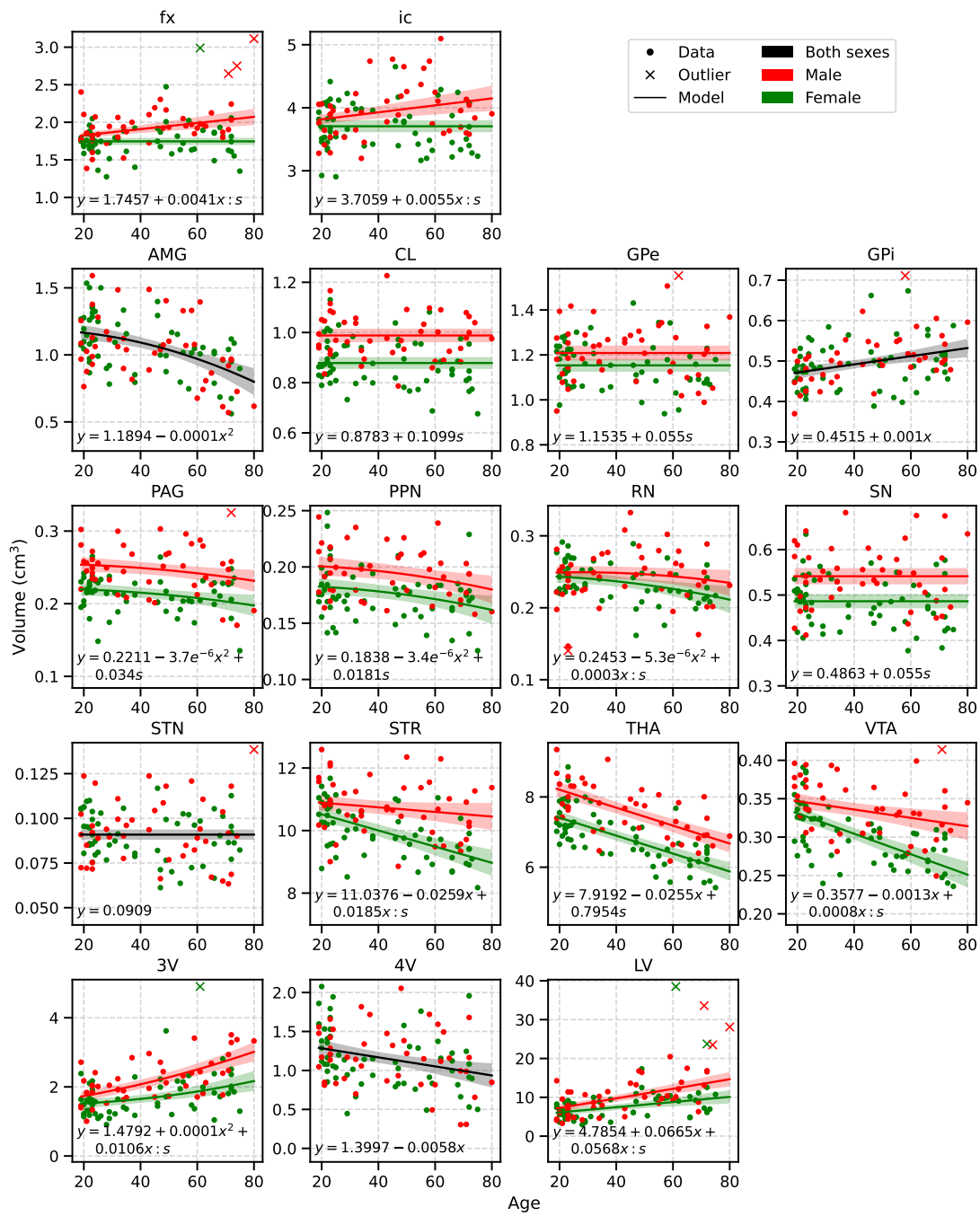


Figure S12: Age-related change in volume for all structures. Equations are the parameterized winning models, with x referring to age, and s to sex (dummy coded; 0 = female, 1 = male), and colons indicate interactions. Shaded areas indicate 95% confidence intervals of the winning model predictions

References

- Bazin, P.-L., Alkemade, A., Mulder, M. J., Henry, A. G., & Forstmann, B. U. (2020). Multi-contrast anatomical subcortical structures parcellation. *eLife*, *9*, 1–23. <https://doi.org/10.7554/eLife.59430>
- Bazin, P.-L., Weiss, M., Dinse, J., Schäfer, A., Trampel, R., & Turner, R. (2014). A computational framework for ultra-high resolution cortical segmentation at 7 Tesla. *NeuroImage*, *93*, 201–209. <https://doi.org/10.1016/j.neuroimage.2013.03.077>
- Gowland, P. A., & Bowtell, R. (2007). Theoretical optimization of multi-echo fMRI data acquisition. *Physics in Medicine and Biology*, *52*(7), 1801–1813. <https://doi.org/10.1088/0031-9155/52/7/003>
- Hallgren, B., & Sourander, P. (1958). The Effect of Age on the Non-Haemin Iron in the Human Brain. *Journal of Neurochemistry*, *3*(1), 41–51. <https://doi.org/10.1111/j.1471-4159.1958.tb12607.x>
- Kundu, P., Voon, V., Balchandani, P., Lombardo, M. V., Poser, B. A., & Bandettini, P. A. (2017). Multi-echo fMRI: A review of applications in fMRI denoising and analysis of BOLD signals. *NeuroImage*, *154*(March), 59–80. <https://doi.org/10.1016/j.neuroimage.2017.03.033>
- Meterer, R., & Möller, H. E. (2018). Quantifying the myelin and iron contents of the brain in vivo using a linear model of relaxation. *Proceedings of the International Society for Magnetic Resonance in Medicine*, *26*.
- Miletić, S., Bazin, P.-L., Weiskopf, N., van der Zwaag, W., Forstmann, B. U., & Trampel, R. (2020). fMRI protocol optimization for simultaneously studying small subcortical and cortical areas at 7 T. *NeuroImage*, *219*(May). <https://doi.org/10.1016/j.neuroimage.2020.116992>
- Poser, B. A., Versluis, M. J., Hoogduin, J. M., & Norris, D. G. (2006). BOLD contrast sensitivity enhancement and artifact reduction with multiecho EPI: Parallel-acquired inhomogeneity-desensitized fMRI. *Magnetic Resonance in Medicine*, *55*(6), 1227–1235. <https://doi.org/10.1002/mrm.20900>
- Posse, S., Wiese, S., Gembris, D., Mathiak, K., Kessler, C., Grosse-Ruyken, M. L., Elghahwagi, B., Richards, T., Dager, S. R., & Kiselev, V. G. (1999). Enhancement of BOLD-Contrast Sensitivity by Single-Shot Multi-Echo Functional MR Imaging. *Magnetic resonance in medicine*, *42*(1), 87–97.
- Puckett, A. M., Bollmann, S., Poser, B. A., Palmer, J., Barth, M., & Cunnington, R. (2018). Using multi-echo simultaneous multi-slice (SMS) EPI to improve functional MRI

of the subcortical nuclei of the basal ganglia at ultra-high field (7T). *NeuroImage*, 172(May 2017), 886–895. <https://doi.org/10.1016/j.neuroimage.2017.12.005>

Randall, L. O. (1938). Chemical Topography of the Brain. *Journal of Biological Chemistry*, 124(2), 481–488.